Accurate Estimation of Pulmonary Nodule's Growth Rate in CT Images with Nonrigid Registration and Precise Nodule Detection and Segmentation

Yuanjie Zheng[1] Chandra Kambhamettu[1] Thomas Bauer[2] Karl Steiner[3]
zheng.vision@gmail.com, chandra@cis.udel.edu, TBauer@christianacare.org, ksteiner@UDel.Edu

[1]Video/Image Modeling and Synthesis (VIMS) Lab.
Department of Computer Science, University of Delaware, Newark, DE, USA
[2]Helen F. Graham Cancer Center, Christiana Care Health Services, Newark, DE USA
[3]Department of Electrical Engineering, University of Delaware, Newark, DE USA

Abstract

We propose a new tumor growth measure for pulmonary nodules in CT images, which can account for the tumor deformation caused by the inspiration level's difference. It is accomplished with a new nonrigid lung registration process, which can handle the tumor expanding/shrinking problem occurring in many conventional nonrigid registration methods. The accurate nonrigid registration is performed by weighting the matching cost of each voxel, based on the result of a new nodule detection approach and a powerful nodule segmentation algorithm. Comprehensive experiments show the high accuracy of our algorithms and the promising results of our new tumor growth measure.

1. Introduction

Lung cancer is worldwide a common cause of cancer death, accounting for 18% of all deaths from cancer. Each year, approximately 1.4 million people are diagnosed with lung cancer [2]. Early detection and treatment of lung cancer has proven to significantly improve the survival rate. To aid in early detection, Computed Tomography (CT) chest screening is popularly used due to its high resolution, reduced scanning time and affordability. With the CT imaging, the detected pulmonary nodules larger than 1 cm in largest dimension have a higher likelihood of malignancy. Otherwise, the nodule is more commonly benign but the malignancy cannot be precluded. The challenge for the radiologist is to correctly identify the few malignant lesions among numerous small benign nodules.

The volumetrically determined growth rate [8, 17] of pulmonary nodule has been reported to be extremely useful in distinguishing between benign and malignant pulmonary nodules, among the different features [16] proposed in the CT imaging based Computer-Aided Diagnosis (CAD). Most methods [12, 17, 8] for computing the growth rates are based on the scheme that the nodules in the images scanned at different times are first segmented independently and then the growth rate is computed based on the volumetric (or diametral) measurements of the segmented nodules. One weakness in the traditional methods is that the inspiration level is not considered although its change can cause unexpected variability to growth rate's computation [5]. The inspiration can lead to more than $\pm 12\%$ volume change of lung, which can bring in significant errors to the growth rate's computation. Another weakness of many previous methods [17, 16, 3] is the inter-observer and intra-observer variability [3] because they rely on manual segmentations. Therefore, it is necessary to account for the inspiration level differences and to provide an automatic and accurate segmentation tool for lung nodule in order to compute accurate growth rates.

In this paper, in order to compute an accurate growth rate for pulmonary nodule, we propose a new tumor growth measure that can account for the nodule deformation caused by the different inspiration levels in two CT scans, and a new scheme to compute the measure. The scheme is founded on the accurate nonrigid registration of the CT images scanned at different times, which provides the quantitative measurement of the nodule deformation caused by the different inspiration levels.

In order to obtain an accurate nonrigid registration, we propose to alleviate the unexpected nodule expanding/shrinking effect [15] caused in the nonrigid registration process by weighting voxels in the matching cost of registration based on the nodule detection results. This unexpected deformation is caused by the large driving force due to the tumor intensity difference caused by the tumor

978-1-4244-3993-5/09/$25.00 ©2009 IEEE

growth. As a result, the small nodule will be nonlinearly deformed to the larger one. This deformation is not caused by lung's deformation but wrongly by the registration algorithm. It can bring in significant errors to the later tumor growth's computation.

For the registration and tumor growth's computation, we also introduce a new automatic nodule detection method and a powerful nodule segmentation approach. Our nodule detection is a template matching technique based on a series of representative templates identified efficiently with the affinity propagation [4] and a newly defined distance between template and local image patch. The segmentation approach is accomplished by solving a Markov Random Field (MRF) with graph cut [18] which was reported to be extremely efficient.

Comprehensive experiments show the high accuracies of our nodule detection, segmentation and registration algorithms, and show the promising results of our new tumor growth measure.

2. Previous Work

There exist different models to describe the tumor growth rate, such as the exponential growth process [8], and the doubling time [17], etc. The doubling time is probably the most widely used measure. One main disadvantage in most previous measures is that the tumor deformation caused by the lung's deformation between different inspiration levels can not be handled in tumor growth's computation.

For lung nodules' detection in CT data, two main types of methods have already been reported: the filtering or template matching based methods [19, 20, 1, 9], and the training based methods [7], both frequently followed by some post processing. With the first method, nodule regions are detected by thresholding the convolved values of images using selected filters or templates. The weakness of these methods is that the filters or the templates need to be predefined based on some prior knowledge which are usually expressed explicitly by functions such as Gabor or Gaussian, etc. In practice, it is very difficult to pre-design functions to fully and robustly represent the various nodules. Also, due to the possiblely large number of templates, the speed is often slow. For the training based methods, neural networks [7] or support vector machine (SVM) are usually applied with some representative features of lung nodule, such as texture etc. Unfortunately, the results highly depend on the characteristics of the training and testing examples, and on the features used in the training and testing processes. Moreover, to obtain accurate classification, a large training set is needed, resulting in slow speed [20]. With the two kinds of existing methods, although the sensitivity of nodule detection can be high, the specificity is relatively low.

For the accurate segmentation of pulmonary nodule, besides the widely used manual segmentation [17, 16, 3], there are also some algorithms [12, 8] proposed to reach high accuracies. However, some modern segmentation techniques like the graph cut [18] are worthy to try because of their better reported performances.

3. Measuring Tumor Growth

In order to account for the nodule deformation caused by the inspiration level's difference in the computation of nodule growth rate, we modify the doubling time [17] to a new measure called the adaptive doubling time (ADT). Other tumor growth rate measures can also be modified in a similar way.

The original doubling time [17] is computed as

$$DT = \frac{\ln 2 \cdot \delta t}{\ln\left(\frac{V_2}{V_1}\right)} \tag{1}$$

where V_1 and V_2 are the nodule's volumetric measurements in the first CT scan and the follow-up one, respectively, and δt denotes the interval between the two CT scans.

The ADT is computed by incorporating the nonrigid transformation $\mathcal{T}$ of the lung scanned at early time to the one scanned at later time through the registration process (will be explained in sec 4) as

$$ADT = \frac{\ln 2 \cdot \delta t}{\ln\left(\frac{V_2}{V_1 \cdot J_n}\right)}, \tag{2}$$

where J_n is the average Jacobian determinant of $\mathcal{T}$ over the voxels in the nodule of the later scan. For any point $\mathbf{x}$ in the nodule, the Jacobian determinant is calculated as

$$J_{\mathcal{T}}(\mathbf{x}) = \begin{vmatrix} \frac{\partial \mathcal{T}_x(\mathbf{x})}{\partial x} & \frac{\partial \mathcal{T}_x(\mathbf{x})}{\partial y} & \frac{\partial \mathcal{T}_x(\mathbf{x})}{\partial z} \\ \frac{\partial \mathcal{T}_y(\mathbf{x})}{\partial x} & \frac{\partial \mathcal{T}_y(\mathbf{x})}{\partial y} & \frac{\partial \mathcal{T}_y(\mathbf{x})}{\partial z} \\ \frac{\partial \mathcal{T}_z(\mathbf{x})}{\partial x} & \frac{\partial \mathcal{T}_z(\mathbf{x})}{\partial y} & \frac{\partial \mathcal{T}_z(\mathbf{x})}{\partial z} \end{vmatrix} \tag{3}$$

where $\mathcal{T}_x$, $\mathcal{T}_y$ and $\mathcal{T}_z$ represent the scalar functions of the transformation in $\mathcal{T}$ in the directions relative to x, y and z axes, respectively.

By incorporating J_n in the ADT in Eq. (2), nodule's deformation caused by the lung's deformation is eliminated, resulting in a more accurate measurement of nodule's growth rate. Note that the lung's deformation is caused by the different inspiration levels, patient motion, or other reasons. Based on $\mathcal{T}$, the Jacobian determinant $J_{\mathcal{T}}(\mathbf{x})$ in Eq. (3) can measure the factor by which the tumor expands or shrinks at $\mathbf{x}$. Obviously, the accuracy of ADT's computation in Eq. (2) relies on the accuracy of $\mathcal{T}$.

4. Image Registration

Given two images $\mathcal{I}$ and $\mathcal{J}$, registration is to find an optimal geometrical transformation $\mathcal{T}$ that models the motion

from $\mathcal{I}$ to $\mathcal{J}$ and constructs the mapping of the voxels (volume pixels) in $\mathcal{I}$ to J. The optimal $\mathcal{T}$ is found by maximizing a similarity measure between the overlapping regions of the transformed image $\mathcal{T}(\mathcal{I})$ of $\mathcal{I}$ and J.

The transformation $\mathcal{T}$ in our registration algorithm is composed of a global transformation $\mathcal{T}_\mathcal{G}$ and a local transformation $\mathcal{T}_\mathcal{L}$. For an image point $\mathbf{x} = (x, y, z)^T$ in the 3D image $\mathcal{I}$, where x, y and z are the coordinates, we then have

$$\mathcal{T}(\mathbf{x}) = \mathcal{T}_\mathcal{G}(\mathbf{x}) + \mathcal{T}_\mathcal{L}(\mathbf{x}). \quad (4)$$

The global transformation $\mathcal{T}_\mathcal{G}$ is set as the affine transformation, and the parameters are estimated by the iterative multi-resolution search strategy [13] with the Sum of Squared Difference (SSD) similarity measure.

The local transformation $\mathcal{T}_\mathcal{L}$ is given by the free-form deformation (FFD) model based cubic B-splines [13]. The basic idea of the FFD based B-splines is to deform the image through manipulating an underlying lattice of uniformly spaced control points (CPs). The deformation of any voxel can be obtained through interpolating some CPs' displacements. The parameters to be solved for this model are the displacements of the CPs. Details of the model can be found in [13].

The estimation of the local transformation can be formulated as the minimization of an energy function. Our energy function has two terms: a data term E_d to characterize the similarity between the transformed image and the target image, driving force behind the registration process that aims to minimize the matching cost between the two images; and a smoothness term E_s to regularize the transformation field, discouraging certain improbable or impossible transformation. It is written as

$$E = E_d + \lambda_r E_s = \sum_{p \in \mathcal{I}'} C\Big(\mathcal{I}'(p) - \mathcal{J}(p)\Big) + \lambda_r \sum_{p \in \mathcal{I}'} \sum_{p' \in \mathcal{N}_p} \|\mathcal{T}_\mathcal{L}(p) - \mathcal{T}_\mathcal{L}(p')\|^2 \quad (5)$$

where $\mathcal{I}' = \mathcal{T}_\mathcal{L}(\mathcal{I})$, $\mathcal{I}'(p)$ means the image value of voxel p in $\mathcal{I}'$, C models the matching cost, $\mathcal{N}_p$ represents the neighboring voxels of p, $\|\cdot\|$ is the L_2 norm, λ_r is an adjusting parameter (e.g. 0.01) balancing the two terms.

One key element in registration is the specification of E_d in Eq. (5). The traditional image similarity measure like the SSD can cause the nodule expanding/shrinking problem [15]. It is caused by the large driving force from the intensity variations due to the tumor growth. It results in the unexpected mapping of the small nodule to the large one, leading to large errors to the tumor growth's computation.

To solve the tumor expanding/shrinking problem, we compute the matching cost in Eq. (5) as

$$C\Big(\mathcal{I}'(p) - \mathcal{J}(p)\Big) = (1 - \alpha_p) \cdot \big(\mathcal{I}'(p) - \mathcal{J}(p)\big)^2 \quad (6)$$

where α_p is a value with range in $[0\ 1]$ representing the probability of voxel p belonging to nodule. The value of α_p will be determined by the nodule detection process in sec 5.

With the matching cost in Eq. (6), the driving forces of the reliable non-nodule voxels in the registration are very large because their α values are very small, while the driving forces from the unreliable nodule regions are very small because their α values are larger. As a result, the non-nodule voxels plays a much more important role in the computations of the CPs' displacements than the nodule. Please note that the smoothness term in Eq. (5) can bring in accurate deformations to nodule voxels although nodule's intensities may not be used at all in the registration process.

5. Nodule Detection and Segmentation

To determine α_p in Eq. (6), we need the probability value of each voxel belonging to the nodule. This is done by the nodule detection and segmentation process in this section.

For the template matching based techniques in nodule detection, we believe that better nodule templates can help improve the detection accuracy, and more advanced segmentation techniques can produce more precise nodule regions. Better nodule templates should be able to fully and concisely explain the main characteristics of the nodules. They should not only be able to represent the large variations of nodule appearances but also distinguish nodules from other tissues such as vessels.

We propose a new powerful tool for automatic detection and segmentation of lung nodules in CT data. We focus on selecting better nodule templates to improve detection accuracy and use more advanced segmentation technique to improve the segmentation accuracy. To accomplish this, we identify the representative nodule templates from many pre-selected local patches in nodules by utilizing the affinity propagation [4]. We then perform the nodule detection based on template matching using a newly proposed conjugate norm, and the nodule regions' segmentation by solving a Markov Random Field (MRF) with graph cut [18].

Our detection and segmentation approach consists of four steps: the identification process to find the representative nodule templates, the template matching process to detect nodules, the segmentation process to refine the detected regions, and the false positives reduction process to further improve the detection results. In the following, we provide the details of the first three steps. For the final step, we used a similar method to [19].

5.1. Identifying Representative Nodule Templates

We select randomly many local patches in pulmonary nodules and identify a series of representative nodule templates with affinity propagation [4]. The identified repre-

sentative nodule templates can express concisely and fully the main information of the patches.

Before explaining the technique of affinity propagation, we explain more on how to represent a nodule patch. A simple way is to use directly the concatenated vector by the pixels' intensities. However, this method is sensitive to image translation, rotation, noise and other variations caused by the possibly different scanning conditions. In this paper, we describe a nodule patch with some features which are invariant to translation and rotation etc, and use the concatenated feature vectors, denoted by $\{\bar{F}_i,\ i = 1 \cdots N_q\}$, to represent the N_q randomly selected nodule patches from the training data.

Affinity propagation [4] was designed to find an optimal set of clusters, given large noisy data sets, i.e. $\{\bar{F}_i,\ i = 1 \cdots N_q\}$ in our case. It can detect special data points called exemplars, and connects every data point to the exemplar that best represents it. Affinity propagation is able to efficiently and quickly find the exemplars in a few minutes, for which it would normally take hundreds of hours of computer time using other methods. The optimal set of exemplars found by affinity propagation is the one for which the sum of similarities of each point to its assigned exemplars is maximized. The exemplars found from nodule patches are used in this paper as the representative nodule templates, denoted by $\{\bar{T}_i,\ i = 1 \cdots N_t\}$.

The input for affinity propagation is a list of similarities between a pair of data points, i.e, the feature vectors for nodule patches in our case. We compute the similarity between two nodule patches indexed by i and j as the negative squared distance between the two corresponding features vectors:

$$S(i,j) = -dist_{ap}(\bar{F}_i, \bar{F}_j)^2 \tag{7}$$

where the computation of the distance between the two features depends on the kinds of features we are using. Different features may have different definitions of the distance.

We currently use two kinds of features for describing a nodule patch: the probability density function (PDF) of intensity values in the patch [20] and the Gabor texture features [14]. We hence represent the features vector for a nodule patch i as $\bar{F}_i = [\bar{F}_i^{pdf}\ \bar{F}_i^{gab}]^T$. For the former features, the distance between two PDFs, e.g. $\bar{F}_i^{pdf}$ and $\bar{F}_j^{pdf}$, is measured by their absolute Kullback-Leibler (K-L) divergence that describes the relative entropy between the two PDFs, denoted by $\mathcal{D}_{kl}\left(\bar{F}_i^{pdf}, \bar{F}_j^{pdf}\right)$. The latter features (Gabor) are translation and rotation invariant. The number of Gabor textures is $N_o \times N_f$ where N_o is the number of orientations within a period of π and N_f represents the radial frequencies. We set $N_o = 4$ and $N_f = 4$ in our experiments. The distance between two Gabor features' vectors, e.g. $\bar{F}_i^{gab}$ and $\bar{F}_j^{gab}$ is simply the absolute Euclidean distance, denoted by $\mathcal{D}_{eu}\left(\bar{F}_i^{gab}, \bar{F}_j^{gab}\right)$. The distance in equation (7) is therefore defined as

$$dist_{ap}(\bar{F}_i, \bar{F}_j) = \lambda_d \mathcal{D}_{kl}\left(\bar{F}_i^{pdf}, \bar{F}_j^{pdf}\right) + (1-\lambda_d)\frac{\mathcal{D}_{eu}\left(\bar{F}_i^{gab}, \bar{F}_j^{gab}\right)}{1+\mathcal{D}_{eu}\left(\bar{F}_i^{gab}, \bar{F}_j^{gab}\right)} \tag{8}$$

where λ_d is a parameter taking value between $[0\ 1]$ to weigh the density and texture of the nodule patch differently. We set $\lambda_d = 0.5$ in our experiments. Note that D_{kl} is a value between $[0\ 1]$ and $\frac{\mathcal{D}_{eu}\left(\bar{F}_i^{gab}, \bar{F}_j^{gab}\right)}{1+\mathcal{D}_{eu}\left(\bar{F}_i^{gab}, \bar{F}_j^{gab}\right)}$ normalizes D_{eu} to $[0\ 1]$.

Affinity propagation views each data point as a node in a network, and searches for exemplars by recursively transmitting two kinds of real-valued messages along edges of the network until convergence. Here edge in the network means the connection between two neighbor nodes. In our case, any two data points are considered connected. The first kind of message is the "responsibility" sent from each data point to candidate exemplar, reflecting the accumulated evidence for suitability of this candidate exemplar to serve as exemplar for the data point. The other kind of message is the "availability" sent from candidate exemplar to a data point, reflecting the evidence of how appropriate it would be for the data point to choose this candidate exemplar as exemplar. The definitions of the two messages are given in [4]. The message transmission of affinity propagation can be easily performed with the technique in "belief propagation", designed in the study of inference problems [11].

With the affinity propagation above, we find N_t representative nodule templates $\{T_i,\ i = 1 \cdots N_t\}$, which contain the most important information of nodules' appearance in the training data.

5.2. Detecting Nodules using Template Matching

Given the representative nodule templates, various methods can be applied to detect the nodules from a CT chest image. A simple way is to convolve the given CT image with T_i, and threshold the convolved values. This way is limited in practice because it is sensitive to the translation, rotation and other variations as explained above. We can also use the intensities of the representative nodule templates as training data and then utilize *k*-NN to perform detection [20]. This method has the same problems as the previous one. In addition, the possibly large number of pixels in the template may cause problems in the detection process.

In this paper, we introduce two approaches which are much more robust. We name them *Match#1* and *Match#2*, respectively. The *Match#1* approach computes the normalized distance, denoted by $dist_{match1}$, of a local patch centered at an arbitrary pixel in the CT chest image and a rep-

resentative nodule template. This is performed using the equation (8), based on the PDF and Gabor features, as explained in the last section. The pixels with distance below a threshold to any representative template are treated as nodule pixels. The *Match#2* approach uses a conjugate norm instead of the conventional Euclidean norm of the intensity vectors to measure the distance between a representative nodule template and a local patch. The conjugate norm is computed based on the Locality Preserving Projections (LPP) [6].

In the *Match#2* method, we consider the representative nodule templates and the local patches (having same size) as points in a high dimensional space spanned by the intensities of the pixels in each template or patch. We believe that the "intrinsic dimensionality" of the data points in the higher dimensional space is much lower than the number of pixels in the templates or patches and perform dimensionality reduction using LPP. We then perform template matching in the low-dimensional space.

LPP can be seen as an alternative to Principal Component Analysis. Although it is a linear dimensionality reduction algorithm, it can discover the nonlinear structure of the data manifold in the high dimensional space. The solution of the LPP algorithm is obtained by solving a generalized eigenvector problem, and is a matrix Q in size $N_e \times N_x$ where N_e denotes the number of eigenvectors and N_x is the number of pixels in the patch. Each row of Q is an eigenvector, and contains the information of an axis of the low-dimensional space. With Q, we define the distance between a representative template i and a local patch j as a conjugate norm

$$\mathcal{D}_{coj}(\bar{Z}_i, \bar{Z}_j) = (\bar{Z}_i - \bar{Z}_j)^T Q^T Q (\bar{Z}_i - \bar{Z}_j) \qquad (9)$$

where $\bar{Z}_i$ and $\bar{Z}_i$ are the concatenated vectors of the intensities in the corresponding patches. As in equation (8), we can normalize $\mathcal{D}_{coj}$ to $[0\ 1]$ and denote it by

$$dist_{match2}\left(\bar{Z}_i, \bar{Z}_j\right) = \frac{\mathcal{D}_{coj}\left(\bar{Z}_i, \bar{Z}_j\right)}{1 + \mathcal{D}_{coj}\left(\bar{Z}_i, \bar{Z}_j\right)}. \qquad (10)$$

To compute LPP, we use the *k*-nearest neighbors to construct the graph and the "simple-minded" way for specifying the weights of the edges in the graph. Details can be found in [6].

Our *Match#2* matching approach is composed of three steps. We first select N_l local patches which are distributed randomly over the given CT image. We then run the LPP algorithm on the N_l patches plus the N_t representative nodule templates to obtain the matrix Q. We finally perform template matching by dropping off some of the minor eigenvectors in Q and comparing the local patch centered at an arbitrary pixel with all the representative templates using equation (9). The pixels whose value of distance, $dist_{match2}$, to any template is below a threshold are treated as corresponding to a nodule.

5.3. Segmentation of Nodule by Solving an MRF

The connected areas of nodule detection results using methods in last section usually cannot accurately determine the nodules' boundary. We use graph cut [18] as a segmentation process to refine each detected nodule region by solving a Markov Random Field (MRF) problem. The segmentation is performed in a rectangular region obtained by expanding the bounding box of the detected nodule regions for 25 pixels in both row and column directions of the image.

Before performing the graph cut, we concatenate the intensities in a local window centered at a pixel as its intensity vector, and project the vector onto the first 3 eigenvectors in Q (obtained in last section). We therefore get 3 feature values for each pixel and use them to perform segmentation.

Our graph cut algorithm models nodule pixels and background pixels both with three Gaussian distributions of the three features plus intensity. The algorithm recursively estimates the Gaussian parameters and assigns each pixel to a class. More details related to graph cut can be found in [18].

To compute α_p in Eq. (6) based on the matching distances in sec 5.2 and the segmentation result in sec 5.3, if voxel p is not in the segmented nodule region, we set α_p to zero, and otherwise, we set $\alpha_p = 1 - dist(p)$ where $dist(p)$ means voxel p's value of $dist_{match1}$ or $dist_{match2}$ as explained in sec 5.2.

6. Results

Because the computation of our tumor growth measure ADT in sec 3 relies on the result of image registration in sec 4, and the registration process needs the results of nodule detection and segmentation in sec 5, we validate the three processes in the reverse order.

For all the CT pulmonary data sets in our experiments, the size is $512 \times 512 \times 360$, the resolution is $0.62 \times 0.62 \times 1$ mm^3, and the time interval between the two scans ranged from 45 days to 735 days.

6.1. Validation on Nodule Detection and Segmentation

In order to validate our nodule detection and segmentation algorithms, we chose 10 clinical cases, including 7 solid nodules and 5 ground glass opacity (GGO) nodules, and consisting of 85 slices of solid nodules and 53 slices of GGO nodules. The ground-truth nodule regions were specified by a trained rater. We evaluate the performances in a leave-one-out cross-validation (LOOCV) fashion. LOOCV involves using a single clinical case from the 10 clinical

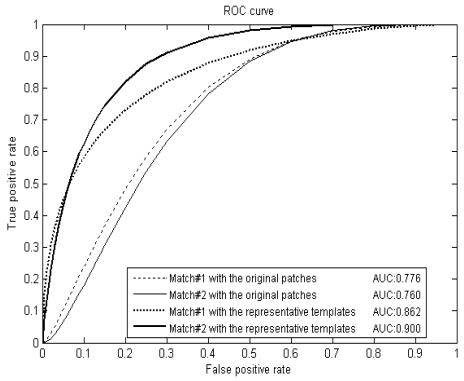

(a)

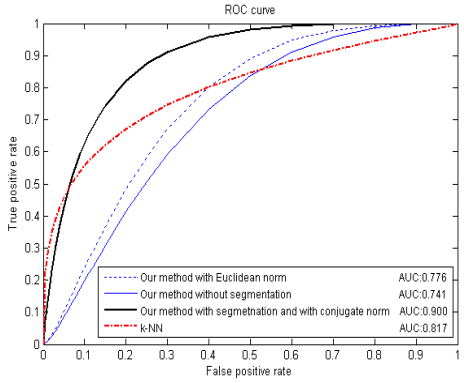

(b)

Figure 1. (a) ROC curves of our *Match#1* and *Match#2* algorithms with and without identifying the representative templates. (b) ROC curves of our *Match#2* algorithm with and without graph cut segmentation, with the Euclidean norm, and with the proposed conjugate norm, and of the *k*-NN algorithm.

cases as the validation data (testing data), and the remaining cases as the training data. LOOCV repeats this such that each case is used once as the validation data.

From the training data, we chose about $N_q = 600$ nodule patches of size 9×9 in each repeat of the LOOCV process, and from which about $N_t = 23$ representative nodule templates were identified. In addition, the detected regions whose area is less than 5 mm^2 were dropped off before the segmentation-based refinement process in our experiments.

We fit the binormal receiver operating characteristic (ROC) curve with the ROCKIT algorithm [10] and use the area under the curve (AUC) to measure the performance of our approach. ROC curve measures the false positive rate and the true positive rate of the obtained nodule pixels as we change the discrimination threshold of the distance $dist_{match1}$ or $dist_{match2}$.

We first validate the effectiveness of the representative nodule templates identified by our method. We draw the ROC curves of our methods with the representative nodule templates, and without them but instead by treating all of the

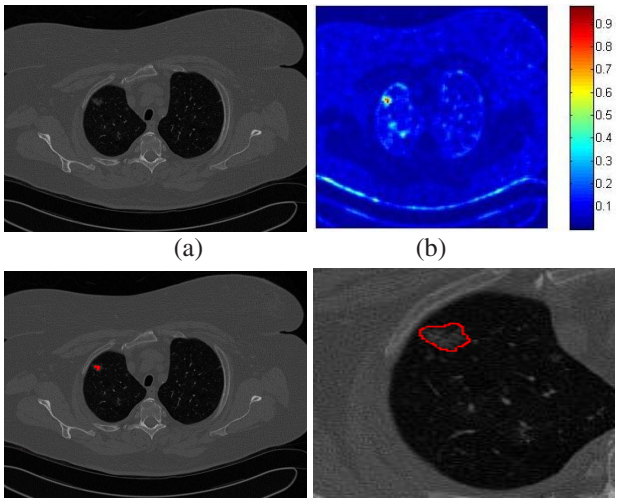

(a) (b) (c) (d)

Figure 2. Demonstration of the performances of our nodule detection and segmentation algorithms. (a) One slice of CT chest image. (b) Color-coded correlation values in our template matching. (c) Nodule detection result shown by the region in red color. (d) Segmentation result show by the curve in red color.

selected nodule patches as templates, in Fig. 1 (a). For the two cases, the proposed conjugate norm was used. From the results, we can see that the representative nodule templates improve the detection accuracy. Moreover, we find that the computational cost spent in the template matching process can be reduced by about 12 folds in our experiments. We illustrate the detection and segmentation results on a slice using our method with *Match#2* in Fig. 2.

We also illustrate the improvement of our methods by using the proposed conjugate norm, and by using the segmentation-based refinement process. For both, the identified representative nodule templates were used. For the former one, we plot the ROC curves with the conventional Euclidean norm and the proposed conjugate norm in Fig. 1 (b). Note that the segmentation-based refinement was used. From the results, we can see that the proposed conjugate norm greatly improves the accuracy. For the latter one, we draw the ROC curves without the segmentation-based refinement process and with it in Fig. 1 (b). Note that the Euclidean norm was used in the template matching. From the results, we can see that the segmentation with graph cut can improve the nodule detection accuracy. The improvement can also be observed in Fig. 2.

We finally compare our method with *k*-NN. *k*-NN was ran by training using about 50 manually chosen exemplar 9×9 nodule patches and testing on the test images in each repeat of the LOOCV. From the ROC curves of *k*-NN and our method in Fig. 1 (b), we can see that our method based on the identification of the representative nodule templates behave much better than *k*-NN training based on the manu-

ally selected nodule patches.

6.2. Validation of Image Registration

To validate the effectiveness of our matching cost (Eq. (6)) in handling the nodule deformation caused by the expanding/shrinking problem in the nonrigid registration process, we ran our algorithms on 11 pairs of CT scans and computed the nodule volume changes. Each pair consists of an early scan and a follow-up scan, between which the nodule's size bears obvious differences and the inspiration levels are guaranteed to be similar. The nodule volume change between the two scans is computed as the percentage of the absolute nodule volume's difference relative to the nodule volume in the early scan. Note that there is a small nodule deformation caused by the inspiration level difference in our data sets. In our experiments, we set the control points' spacing as 8mm. The conjugate norm was used in nodule detection for the registration with our matching cost function in Eq. (6).

From our experiments, we found that the mean value of the nodule volume changing percentages is 13.98% without the registration process, 0.18% if computed after registration with the traditional SSD, and 14.21% if computed after registration with our new matching cost in Eq. (6). From the results, we can see that the nonrigid registration with the traditional SSD measure bears significant expanding/shrinking effects on nodule. Obviously, this unexpected nodule deformation can bring in large errors in tumor growth's computation. In contrast, the result of our method is very similar to the one without registration, meaning that our method can efficiently handle the expanding/shrinking. The comparisons with one example pair of scans are shown in Fig. 3.

6.3. Assessment on Tumor Growth Measure

Experiments performed to evaluate our adaptive doubling time (ADT) measure on tumor growth was designed to compare the differences with the traditional doubling time (DT). Two CT scans were obtained for each of 10 small benign pulmonary nodules that have been observed to have no significant growth by an experienced rater. We computed the DT values based on the manual segmentations of the nodules and the ADT based on the new scheme proposed in this paper. The mean and standard deviation of DTs are 1098 days and 879 days, and the values of ADTs are 25901 days and 223 days. It means that ADT is a better and more stable measure than DT. It is because the nodule deformation caused by the inspiration level's difference can be accounted in ADT but can not in DT.

We also compute the ADT measure values on 9 malignant nodules, for each of which, two CT scans were obtained. We found that the resulting ADT values range from 45 days to 184 days.

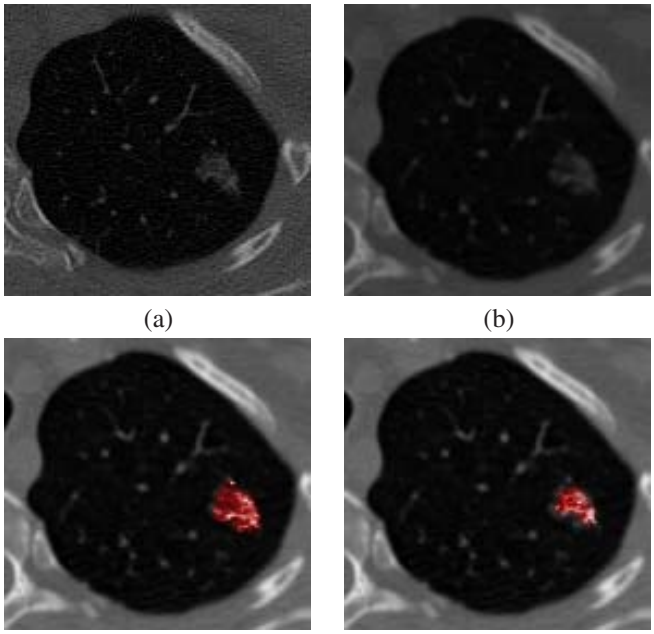

Figure 3. The new matching cost in Eq. (6) can efficiently handle the nodule's expanding/shrinking problem commonly caused in the nonrigid registration process with the traditional cost measures like SSD. (a) and (b) show a nodule detected during the initial CT scan and a follow-up CT scan, respectively. (c) and (d) show the overlapping results of the nonrigidly aligned small tumor over the large tumor. (c) is obtained with the traditional SSD measure while (d) is with our matching cost measure in Eq. (6).

7. Conclusion and Future Work

We proposed a new tumor growth measure called adaptive doubling time (ADT), which can account for the tumor deformation caused by the inspiration level's difference. In order to compute ADT, we propose a powerful nonrigid lung registration algorithm. The new algorithm can handle the tumor expanding/shrinking problem caused in many traditional nonrigid registrations. This is accomplished by weighting of the matching costs of each voxel based on a newly proposed nodule detection process and a powerful segmentation refinement process.

However, as also pointed by Reeves *et al*. [12], the evaluation of the tumor growth measures is not an easy task. Although we have achieved promising results from the ADT with 10 benign tumors, more data is necessary for the validation, and more complete evaluations with well established growth rates of malignant nodules are needed.

ACKNOWLEDGEMENT

This publication was made possible by Grant Number 2 P20 RR016472-08 under the INBRE program of the National Center for Research Resources (NCRR), a component of

the National Institutes of Health (NIH).

References

[1] K. T. Bae and et al. Pulmonary nodules: Automated detection on CT images with morphologic matching algorithm preliminary results. *Radiology*, 236:286–293, 2005.

[2] Cancer Research UK. Commonly diagnosed cancers worldwide. Technical report, Cancer Research UK, http://info.cancerresearchuk.org/cancerstats/geographic/world/commoncancers/, April 2005.

[3] J. J. Erasmus, G. W. Gladish, L. Broemeling, B. S. Sabloff, M. T. Truong, R. S. Herbst, and R. F. Munden. Interobserver and intraobserver variability in measurement of noncsmall-cell carcinoma lung lesions: Implications for assessment of tumor response. *Journal of Clinical Oncology*, 21:2574–2582, 2003.

[4] B. J. Frey and D. Dueck. Clustering by passing messages between data points. *Science*, 315:972–976, 2007.

[5] H. A. Gietema, C. M. Schaefer-Prokop, W. P. T. M. Mali, G. Groenewegen, and M. Prokop. Pulmonary nodules: Interscan variability of semiautomated volume measurements with multisection CT influence of inspiration level, nodule size, and segmentation performance. *Radiology*, 245:888–894, 2007.

[6] X. He and P. Niyogi. Locality preserving projections. In *Advances in Neural Information Processing Systems 16*, Vancouver, Canada, 2003.

[7] K. G. Kim and et al. Computer-aided diagnosis of localized ground-glass opacity in the lung at CT: Initial experience. *Radiology*, 37:657–661, 2005.

[8] W. J. Kostis, A. P. Reeves, D. F. Yankelevitz, and C. I. Henschke. Three-dimensional segmentation and growth-rate estimation of small pulmonary nodules in helical CT images. *IEEE Trans. Medical Imaging*, 22:1259–1274, 2003.

[9] Y. Lee and et al. Automated detection of pulmonary nodules in helical CT images based on an improved template-matching technique. *IEEE Transactions on Mecial Imaging*, 20:595–604, 2001.

[10] C. E. Metz and et al. Maximum likelihood estimation of receiver operating characteristic (ROC) curves from continuously-distributed data. *Stat. Med.*, 17:1033–1053, 1998.

[11] J. Pearl. *Probabilistic reasoning in intelligent systems: networks of plausible inference*. Morgan Kaufmann Publishers Inc., 1988.

[12] A. P. Reeves, A. B. Chan, D. F. Yankelevitz, C. I. Henschke, B. Kressler, and W. J. Kostis. On measuring the change in size of pulmonary nodules. *IEEE Trans. Medical Imaging*, 25:435–450, 2006.

[13] D. Rueckert, L. Sonoda, I. C. Hayes, D. L. G. Hill, M. O. Leach, and D. J. Hawkes. Nonrigid registration using free-form deformations: Application to breast MR images. *IEEE Transactions on Medical Imaging*, 18:712–721, 1999.

[14] T. Tan. Rotation invariant texture features and their use in automatic script identification. *IEEE Trans. Pattern Anal. Mach. Intell.*, 20:751–756, 1998.

[15] C. Tanner, J. A. Schnabel, D. Chung, M. J. Clarkson, D. Rueckert, D. L. G. Hill, and D. J. Hawkes. Volume and shape preservation of enhancing lesions when applying non-rigid registration to a time series of contrast enhancing MR breast images. In *MICCAI 2000*, pages 327–337, 2000.

[16] D. Wormanns and S. Diederich. Characterization of small pulmonary nodules by CT. *European Radiology*, 14:1380–1391, 2004.

[17] D. F. Yankelevitz, A. P. Reeves, W. J. Kostis, B. Zhao, and C. I. Henschke. Small pulmonary nodules: Volumetrically determined growth rates based on CT evaluation. *Radiology*, 217:251–256, 2000.

[18] R. Zabih and V. Kolmogorov. Spatially coherent clustering using graph cuts. In *CVPR 2004*, volume 2, pages II–437–II–444, 2004.

[19] B. Zhao and et al. Automatic detection of small lung nodules on CT utilizing a local density maximum algorithm. *Journal of Applied Clinical Medical Physics*, 4:248–260, 2003.

[20] J. Zhou and et al. Automatic detection and segmentation of ground glass opacity nodules. In *Medical Image Computing and Computer-Assisted Intervention - MICCAI 2006*, pages 784–791, 2006.